# High Thermoelectric Powerfactor in 2D Crystals of $MoS_2$

Kedar Hippalgaonkar[1, 2, 3, †], Ying Wang[1, †], Yu Ye[1, †], Diana Y. Qiu[2,4], Hanyu Zhu[1], Yuan Wang[1, 2], Joel Moore[2, 4], Steven G. Louie[2,4], Xiang Zhang[1, 2, *]

[1] *NSF Nano-scale Science and Engineering Center (NSEC), 3112 Etcheverry Hall, University of California, Berkeley, California 94720, USA*

[2] *Material Sciences Division, Lawrence Berkeley National Laboratory (LBNL), 1 Cyclotron Road, Berkeley, CA 94720, USA*

[3] *Institute of Materials Research and Engineering, Agency for Science Technology and Research, Singapore, 117602*

[4] *Department of Physics, University of California, Berkeley, California 94720 USA*

*† These authors contributed equally.*

**Correspondence and requests for materials should be addressed to X. Z. (email: xiang@berkeley.edu)*

## ABSTRACT

The quest for high-efficiency heat-to-electricity conversion has been one of the major driving forces towards renewable energy production for the future. Efficient thermoelectric devices require high voltage generation from a temperature gradient and a large electrical conductivity, while maintaining a low thermal conductivity. For a given thermal conductivity and temperature, the thermoelectric powerfactor is determined by the electronic structure of the material. Low dimensionality (1D and 2D) opens new routes to high powerfactor due to the unique density of states (DOS) of confined electrons and holes. 2D transition metal dichalcogenide (TMDC) semiconductors represent a new class of thermoelectric materials not only due to such confinement effects, but especially due to their large effective masses and valley degeneracies. Here we report a powerfactor of $MoS_2$ as large as 8.5 $mWm^{-1}K^{-2}$ at room temperature, which is amongst the highest measured in traditional, gapped thermoelectric materials. To obtain these high powerfactors, we perform thermoelectric measurements on few-layer $MoS_2$ in the metallic regime, which allows us to access the 2D DOS near the conduction band edge and exploit the effect of 2D confinement on electron scattering rates, which result in a large Seebeck coefficient. The demonstrated high, electronically modulated powerfactor in 2D TMDCs holds promise for efficient thermoelectric energy conversion.

## I. INTRODUCTION

An ideal thermoelectric material behaves as an electron-crystal and phonon-glass, allowing a large temperature gradient across it while conducting electricity efficiently to generate a thermoelectric voltage [1]. Significant progress in the thermoelectric performance of materials has been made by exploring ultralow thermal conductivity at high temperature [2] and reducing thermal conductivity by nanostructuring [3], as well as by resonant doping [4] and energy-dependent scattering [5] of electrons. Recently, 2D transition metal dichalcogenides (TMDCs) have shown unique valley-dependent electronic and optical properties [6–10], and also have been theoretically predicted to be superior thermoelectric materials [11–13]. Most theoretical analyses are centered on low lattice thermal conductivity, but the latest calculations suggest that favorable electronic properties of TMDCs also result in an enhanced Seebeck effect [6,14–17], different from gapless, massless carriers in semi-metallic graphene [18–22]. Recent experiments have studied the photo-thermoelectric effect and Seebeck coefficient of monolayer $MoS_2$ at low carrier densities in the insulating regime, but low electrical conductivity limits its powerfactor for thermoelectric applications [23,24]. Here, we examine thermoelectric transport in 2D crystals of few-layer $MoS_2$ at high carrier concentrations in the metallic regime and observe powerfactors, $S^2\sigma$, as large as 8.5 $mWm^{-1}K^{-2}$ in bilayer $MoS_2$, where $S$ is the Seebeck coefficient and $\sigma$ is the electrical conductivity. We use the Seebeck coefficient to probe the 2D density of states (DOS) in both monolayer and bilayer $MoS_2$ and show that it agrees well with first-principles calculations. Moreover, we show that confinement effects on the electronic DOS and scattering rate enhance the Seebeck coefficient in 2D and the bilayer, in particular, has a larger value as a consequence of the higher effective mass and larger valley degeneracy. 2D TMDCs with high powerfactors are promising thermoelectric materials for planar applications such as Peltier cooling devices.

## II. RESULTS

### A. Gate-dependent powerfactor at room temperature

The Seebeck coefficient and electrical conductivity of 2D $MoS_2$ are measured as a function of carrier concentration tuned by a back gate (Fig. 1, see Appendix A: Methods for detailed measurement process). The electron concentration is given by $n = C_{ox}/e\cdot(V_g - V_t)$, where $C_{ox}$ is the capacitance between the channel and the back gate, $e$ is the electron charge, and $V_g$ and $V_t$ are the gate and threshold voltage, respectively. The measured electrical conductivities and Seebeck coefficients of monolayer, bilayer and trilayer $MoS_2$ follow behavior akin to an extrinsically doped semiconductor as shown in Fig. 2. The Seebeck voltage is proportional to the asymmetry of occupied density of states around the Fermi level [5,25]. Hence, with increasing electron concentration, the magnitude of the Seebeck coefficient drops as the Fermi level is pushed closer to the conduction band minimum (CBM). However, the measured powerfactor $S^2\sigma$ increases correspondingly with applied gate voltage $V_g$ due to increasing electrical conductivity illustrated in Fig. 3. The bilayer device exhibits the largest powerfactor $S^2\sigma = 8.5$ $mWm^{-1}K^{-2}$ at $V_g = 104$ V equivalent to a high electron concentration of $n_{2D} \sim 1.06\times10^{13}$ $cm^{-2}$.

The magnitude of the powerfactor is expected to reach a peak and then drop for even higher carrier concentrations as the increasing electrical conductivity is offset by the decreasing Seebeck coefficient [5]. However, for our $MoS_2$ samples, the powerfactor does not peak, as this

optimum carrier concentration is expected to occur at an even higher gate voltage ($n_{2D} \sim 1.31\times10^{13}$ cm$^{-2}$ equivalent to a bulk concentration of $n_{3D} \sim 1\times10^{20}$ cm$^{-3}$ – obtained by considering a bilayer thickness of 1.3 nm), which is limited by the electrical breakdown of the gate oxide in our experiment as shown for a couple of devices in Supplementary Material [26].

The effective mobilities are determined by a standard transistor measurement shown in Fig. 4. The measured effective mobilities at room temperature are 37 cm$^2$V$^{-1}$s$^{-1}$ for the monolayer and 64 cm$^2$V$^{-1}$s$^{-1}$ for the bilayer. The bilayer sample shows the largest electrical conductivity as well as the highest Seebeck. Note that our samples are exfoliated from natural molybdenite crystals, so their initial dopant and impurity levels vary. Hence, the device mobilities differ from sample to sample and are lower than the theoretical estimate (~410 cm$^2$V$^{-1}$s$^{-1}$) [27], which could be due to extrinsic effects such as screening and scattering from the underlying dielectric substrate [16] and impurity levels in individual samples [28]. For phonon-limited theoretical mobility in suspended monolayer $MoS_2$, a powerfactor as large as 28 mWm$^{-1}$K$^{-2}$ is predicted at $n_{2D}=1\times10^{12}$ cm$^{-2}$ [13]; therefore, in principle, the powerfactor of 2D $MoS_2$ can be improved further by making cleaner samples to obtain higher mobility closer to the theoretical limit.

### B. Temperature dependent transport in monolayer $MoS_2$

At high temperatures and high electron concentrations, when the Fermi level is pushed close to the conduction band edge, monolayer $MoS_2$ undergoes an insulator-to-metal transition [14–16]. This metal-like regime for conducting $MoS_2$ is determined by analyzing the conductivity as a function of temperature for different electron concentrations (gate voltages): we study the temperature dependent electrical conductivity from $1.0\times10^{11}$ cm$^{-2}$ to $5.1\times10^{12}$ cm$^{-2}$ for a monolayer $MoS_2$ sample as plotted in Fig. 5(a). The insulator-to-metal transition temperature ($T_{IMT}$) is defined as the temperature at which the measured conductivity changes from increasing with temperature to a metal-like decrease with temperature. This is further corroborated from the mobility as a function of temperature, which changes its slope from 0.3 to ~1.9 at the MIT temperature shown in Fig. 5(b). We thus illustrate the electronic phase diagram of transport in $MoS_2$ in Fig. 6(a) where $T_{IMT}$ is plotted as a function of the carrier concentration. Since this phase diagram is linked to percolation, in the insulating phase, the conductivity follows a relation in temperature given by: $\sigma \propto \exp(-(T_0/T)^{1/3})$ in a 2D system, which fits a Mott Variable-Range-Hopping (m-VRH) model [16,28,29], separate from the first order transition described elsewhere [14,30]. Figure 6(b) shows the measured Seebeck coefficient, which follows a monotonic increase with temperature as $S \propto T^{1/3}$, using Zyvagin's formula for the m-VRH model [31–33], with $S \to 0$ as $T \to 0$ (inset). Similar m-VRH transport phenomenon has also recently been observed in CVD-grown $MoS_2$ for the insulating phase [23], in stark contrast with thermally activated transport mechanism in semiconductors [34,35]. Therefore, from the electronic phase diagram in Fig. 6(a) for high temperatures ($T$>250 K) and large electron concentrations ($n > 2\times10^{12}$ cm$^{-2}$ at 300 K), electrical transport in $MoS_2$ is metal-like and the Mott relation for calculation of the Seebeck coefficient holds. The doping level is not high enough to observe metallic transport behavior at lower temperatures.

### C. Nature of scattering in monolayer and bilayer $MoS_2$

High powerfactors in 2D $MoS_2$ have been predicted to stem from large conduction

band effective masses, leading to a large Seebeck coefficient [13]. In order to better understand the origin of the large Seebeck magnitude for monolayer and bilayer $MoS_2$, we calculate the Seebeck from the linearized Boltzmann Transport Equation (BTE) under the relaxation time approximation, given by:

$$S = \frac{1}{qT}\frac{\int_{E_c}^{\infty}\frac{df_{FD}}{dE}D_{2D}(E).(E-E_F).\tau(E)dE}{\int_{E_c}^{\infty}\frac{df_{FD}}{dE}D_{2D}(E).E.\tau(E)dE} \quad (1)$$

Here, $f_{FD}$ is the Fermi Dirac distribution, $D_{2D}(E)$ is the 2D density of states, $E_F$ is the Fermi Level with respect to the CBM at $E_c$, $q$ is the electron charge, and $\tau(E) = \tau_0 E^r$ is the energy-dependent relaxation time where $r$ is the scattering exponent and depends on the dominant scattering mechanism [36].

1. *Calculating effective mass and density of states in monolayer and bilayer $MoS_2$:*

In order to obtain the density of states used in Equation (1) above, we performed first-principles calculations of the quasiparticle (QP) bandstructure of suspended monolayer and bilayer $MoS_2$ within the GW approximation [37]. The conduction band minimum was found to be at the K and K' points in the Brillouin zone for monolayer $MoS_2$ and along the six-fold degenerate Λ-high-symmetry line (Λ valley) for bilayer $MoS_2$, in good agreement with previous calculations [38–40]. The computed DOS of pristine monolayer and bilayer $MoS_2$ at the GW level show that due to the larger band effective mass and higher degeneracy in the Λ-valley, the DOS of bilayer $MoS_2$ at the CBM is ~4 times larger than the DOS of monolayer $MoS_2$. We included the Mo semicore 4d, 4p and 4s states as valence states for our DFT and GW calculations. The theoretical band structure and density of states calculations were done in a supercell arrangement with a plane-wave basis using norm-conserving pseudopotentials with a 125 Ry wave function cutoff. The distance between repeated supercells in the out-of-plane direction was 25 Å. We fully relaxed the monolayer and bilayer $MoS_2$ structures and included spin-orbit interactions as a perturbation [41,42]. The dielectric matrix was calculated on a 60x60x1 q-point grid with a 25 Ry energy cutoff. 2500 bands were included in the summation over empty states. Dynamical effects in the screening were included with the Hybertsen-Louie generalized plasmon pole model (HL-GPP) [37].

The calculated QP bandstructures of monolayer and bilayer $MoS_2$ are shown in Fig. 7. We find that monolayer $MoS_2$ has a direct bandgap at the K point. In addition to the conduction band minimum (CBM) at K, there is another valley in the conduction band along the Λ-high-symmetry line from Γ to K. We find that the bottom of this Λ valley is 67 meV higher in energy than the K-point and thus unlikely to contribute to the Seebeck at room temperature. We also find that spin-orbit coupling splits the conduction band at K by 2 meV, so we expect that both spin bands will contribute to the transport. We further determine that the effective mass of the lower band (which we will refer to as spin up) is $0.45m_0$, and the effective mass of the upper band (which we will refer to as spin down) is $0.59m_0$, where $m_0$ is the free electron mass. For bilayer $MoS_2$, we ascertain that the CBM occurs along the Λ high-symmetry line. This Λ valley is anisotropic, and its average effective mass is $0.68m_0$. Calculated effective masses, spin-orbit (SO) splitting of the conduction band, and ordering of the conduction band valleys are summarized in Table I. As expected for parabolic bands in 2D, we observe that the DOS is a step function at the conduction band edge in both cases

(Figs. 8a and 8b: The broadening seen in the figures results from a numerical 20meV broadening in the calculation). Thus, in estimating the Seebeck from equation (1) above, we assume that the DOS is constant, given by the value of the DOS at the step edge (dotted vertical lines in Figs. 8a and 8b) and hence energy-independent.

Finally, we explore the possibility that carrier doping, which is known to renormalize the QP band gap, might also change the QP effective masses. We performed an additional GW calculation on doped monolayer $MoS_2$, with a carrier concentration of n=1x10$^{13}$ cm$^{-2}$. We found that QP effective mass of the spin up band in the K valley is unchanged for the spin-up band, while the effective mass of the spin down band decreases by 10%. Thus, the average carrier effective mass decreases by ~0.08 $m_0$ as the doping is increased from 0 to n=1x10$^{13}$ cm$^{-2}$.

2. *Calculation of Seebeck Coefficient and Fermi Level (with respect to the conduction band minimum (CBM):*

In order to calculate the Seebeck coefficient for the monolayer and bilayer samples, the position of the Fermi Level, $E_f$ with respect to the CBM, $E_c$ given by $(E_f - E_c)$ must be known. Given that the doping due to the backgate pushes the 2D $MoS_2$ channels into the degenerate limit (evidenced by the decreasing conductivity with temperature and the linearity of the measured Seebeck as a function of temperature), Fermi-Dirac statistics need to be used. Boltzmann statistics are only valid in the limit that $|E_c-E_f| >> k_BT$, which is not the case in our experiments at high carrier concentrations.

Therefore, in the degenerate limit,

$$n = \int_{E_c}^{\infty} D_{2D}(E) f_{FD}(E) dE \qquad (2)$$

where $D_{2D}(E) = \frac{g_v g_s m^*}{2\pi\hbar^2}$ are the 2D density of states (DOS) ascertained earlier. Here, $g_v$ and $g_s$ are the valley and spin degeneracies respectively and $m^*$ is the band effective mass obtained from the band structure. A summary of the values for monolayer and bilayer are given in Table II.

$f_{FD}(E) = \frac{1}{e^{(E-E_f)/k_BT}+1}$ is the Fermi-Dirac distribution. Let $\varepsilon = (E - E_c)/k_BT$ and $\eta = (E_F - E_c)/k_BT$. Then, equation (2) gives:

$n_{2D} = N_{c,2D} \int_0^{\infty} f_{FD}(\varepsilon) d\varepsilon$, where $N_{c,2D} = D_{2D}.k_BT$ is the effective density of states in two dimensions. Here, $\int_0^{\infty} f_{FD}(\varepsilon) d\varepsilon = F0\eta$ is the 0$^{th}$-order Fermi Integral, which can be evaluated analytically: $F_0(\eta) = \ln(1 + e^{\eta})$.

Therefore, in order to relate the Fermi energy to the carrier density, we use the expression $(E_F - E_c) = k_BT\left(e^{n/N_c} - 1\right)$, where *n* is determined experimentally in the 2D $MoS_2$ channel.

Calculating the Seebeck coefficient as a function of the carrier concentration, *n*, elucidates the dominant scattering mechanism of electrons in the 2D $MoS_2$ channels given by Equation (1). Using the energy-independent DOS, $D_{2D}$, and accounting for the energy-dependent scattering rate, equation (1) can be written as:

$$S = -\frac{k_B}{q}\left[\eta - \frac{(r+2)\int_0^{\infty} f_{FD}\varepsilon^{r+1} d\varepsilon}{(r+1)\int_0^{\infty} f_{FD}\varepsilon^{r} d\varepsilon}\right] \qquad (3)$$

For scattering of acoustic phonons, it has been shown that $\tau(E)$ scales with the density of states [43], thus, r=0 for acoustic phonon-limited scattering in 2D in the single parabolic band model. For charged impurity scattering, the scattering roughly has the energy dependence r=3/2, for a simple model for elastic scattering where the bands are assumed to be

parabolic and the impurity is screened with a Thomas-Fermi type screening in 2D [43]. Typically, r=3/2 is the exponent for electrons scattered by charged impurities in three dimensions, but it can be different for two dimensions depending on the approximations used [36,43,44]. We calculate the Seebeck coefficient for both monolayer and bilayer $MoS_2$ as a function of the carrier concentration, and compare the calculated Seebeck to experimental values for four different devices each (Figs. 8c and 8d respectively). Numerical integration was performed using the function fermi.m in Matlab® [45]. Here, we see that the Seebeck, as calculated from Equation (3), fits the experimental data quite well when r=0, which is consistent with phonon-limited scattering in 2D and captures the relative change in the Seebeck as a function of the carrier concentration induced by the backgate voltage. Finally, our calculations show that given identical carrier concentrations, the magnitude of the Seebeck for the bilayer is larger than that for the monolayer, as a consequence of the larger density of states at the conduction band edge, which stems from both the heavier effective mass as well as a higher valley degeneracy of the CBM at the high symmetry Λ-valley.

Note here that the value of the Seebeck coefficient does not depend on the absolute value of the scattering time, $\tau$. Hence, while the mobility of the samples measured is limited directly by the scattering time, given by $\mu = e\tau/m^*$, the Seebeck is only sensitive to the availability of the DOS near the Fermi energy and the energy-dependence of the scattering term.

Comparing the experimentally measured Seebeck coefficient to theory strongly suggests that the scattering is dominated by electron-phonon scattering. The electron-phonon scattering rate in monolayer has been previously calculated from first principles [27,46]. Over an energy range of 50 meV, the scattering rate in both the K and Λ valleys is indeed constant, with a total scattering rate of roughly $1x10^{13}$ $s^{-1}$ over all phonon modes. However, the mobilities in our samples are lower than the intrinsic phonon-limited mobility of ~410 $cm^2/V.s$ [27]. Our measured mobilities are similar to other measured mobilities for $MoS_2$ on $SiO_2$ [14,17], suggesting that substrate-monolayer coupling may significantly alter the phonon channels available to carriers in $MoS_2$.

## III. DISCUSSION

The Seebeck coefficient is given by integrating the energy dependent relaxation time modulated by a window function defined by $F_{wl}(E,T) = (E-E_F) \times \{-df_{FD}(E,T)/dE\}$, where $E_F$ is the Fermi level and $f_{FD}(E,T)$ is the Fermi-Dirac distribution [47]. This function is odd around $E_F$, with a width of $\sim 2k_BT$ [48]. For doped, metal-like 2D $MoS_2$, as the Fermi level approaches the bottom of the conduction band within this energy width of the window function, the rapidly changing DOS (Fig. 8a and 8c) generates a large asymmetry around the Fermi level, which leads to an enhanced value of the Seebeck coefficient [49,50]. This effect is exacerbated by the large transport effective mass ($m_d^*$), which includes the valley and spin degeneracies. In three dimensions, $m_d^* = (g_v \cdot g_s)^{2/3} \times m^*$ [1,48]. In two dimensions, $m_d^* = (g_v \cdot g_s) \times m^*$; for monolayer $MoS_2$, $g_v = g_s = 2$, and thus the density of states effective mass contributing to transport is $m_{d,1L}^* \sim 2.1m_0$. Bilayer $MoS_2$ has $g_v = 6$ and $g_s = 2$, giving $m_{d,2L}^* \sim 8.1m_0$. These values are significantly larger than conventional thermoelectric materials and indeed are the main reason for our large measured Seebeck coefficients.

The fits to the Seebeck coefficient in Figs 8c and 8d using the full Fermi-Dirac distributions are accurate for carrier concentrations higher than n ~2-4x$10^{12}$

$cm^{-2}$, which is consistent with the phase diagram in Fig. 6a. At lower temperatures and lower carrier concentrations, VRH transport is determined by a localization length up to n ~ $2x10^{12}$ $cm^{-2}$ (Supplemental Material). Bandgap renormalization in monolayer $MoS_2$ at high doping levels (~$1x10^{13}$ $cm^{-2}$) causes the average effective mass to decrease slightly with doping concentration, thus explaining the slight drop in the measured Seebeck coefficient at high carrier concentrations in Fig. 8c. Notwithstanding these minor effects, the scattering exponent ($r = 0$) determined from fitting the calculated Seebeck coefficients to the experimental data as well as the exponent of the temperature-dependent mobility, at high temperatures prove that transport in supported, doped 2D $MoS_2$ (and probably more generally in TMDCs) is limited by phonon scattering at high temperatures.

Despite the excellent agreement of experimental and theoretical Seebeck coefficient, our measured field-effect mobility is still much lower than the calculated, intrinsic value of 410 $cm^2/V.s$ [27] because in the calculation of the intrinsic mobility the total scattering rate is obtained as a sum over all the phonon channels only in pristine monolayer $MoS_2$. It's not surprising, in our case, that the substrate would add additional scattering channels, thus reducing the mobility further. Intriguingly, as the Seebeck coefficient does not depend on the energy-independent magnitude of the scattering time, $\tau_0$, but instead only on the energy-dependent exponent, $r$, there are many avenues to improve the measured powerfactor further by judiciously picking substrates with weak phonon-coupling, as well as improving the quality of the $MoS_2$ channel. The magnitude of the Seebeck coefficient is expected to be even larger when the relaxation time has energy-dependence with r>0 (r=1.5 is plotted for reference in Figs. 8c and 8d), so engineering the dielectric environment to change the dominant scattering mechanism is another possible route to enhance the powerfactor. Like $MoS_2$, other TMDCs [51] and phosphorene [52,53] are expected to simultaneously have large band effective masses and mobilities possibly leading to high values of powerfactor, thus highlighting 2D semiconductor crystals as potential thermoelectric materials. It remains to be seen if the thermal conductivity of these materials can be tuned further, making them directly useful for thermoelectric applications by enhancing the thermoelectric figure-of-merit ZT, although a high powerfactor itself can be utilized for in-plane Peltier cooling [54].

## IV. CONCLUSIONS

Our experiments report the thermoelectric properties of exfoliated 2D crystals of $MoS_2$, and we observe high powerfactors as large as 8.5 $mWm^{-1}K^{-2}$ at room temperature. This is twice as high as commonly used bulk $Bi_2Te_3$, making 2D TMDCs promising candidates for planar thermoelectric applications. The enhanced powerfactor in the metallic regime is attributed to the sizable conductivity in the highly doped crystals and a large Seebeck coefficient stemming from high valley degeneracies and effective masses, especially in the case of the bilayer where a large effective mass at the CBM in the Λ-valley is coupled with a 6-fold valley degeneracy. We measure thermoelectric transport in the highly doped regime for the first time, thus allowing us to access the 2D density of states in TMDCs. Our device configuration allows us to tune the carrier concentration of 2D $MoS_2$, which is difficult in bulk materials, hence providing important insights into thermoelectric transport in these layered materials. The high powerfactor in layered TMDCs provides an exciting avenue to enhance thermoelectric efficiencies and galvanize the growth of thermoelectric devices in the near future.

Note: During the review process, it came to our attention that similar work has been published in Ref [55] with conclusions comparable to what we've obtained, although the effect of increased degeneracy in bilayer and the origin of the enhanced Seebeck is not considered in their study.

## FIGURES

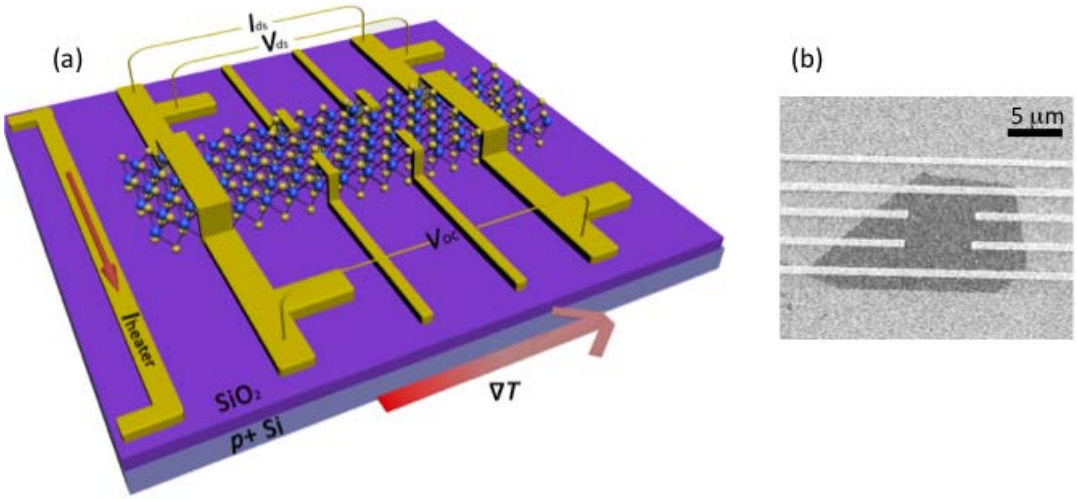


**FIG. 1.** (a) Schematic of the simultaneous measurement of the Seebeck coefficient and the electrical conductivity. The illustration shows a monolayer $MoS_2$, placed on thermally grown $SiO_2$ on a *p*+ silicon substrate. Two-probe electrical conductivity was measured by passing a current through the device ($I_{ds}$) and measuring the drain-source voltage ($V_{ds}$) at each temperature. In order to measure the Seebeck coefficient $S = -V_{oc}/\Delta T$, current was passed through the heater to generate a temperature gradient, $\Delta T$ while the open circuit voltage ($V_{oc}$) was measured. (b) Scanning electron micrograph of an actual device as described in (a). Note, the hall-bar electrodes were used to obtain the ratio of the two-probe to the four-probe electrical conductivities, $\gamma_c = \sigma_{4p}/\sigma_{2p}$ to estimate the contribution due to contact resistance at each temperature. For the monolayer sample, $\gamma_c = 1.98$ at 300 K.

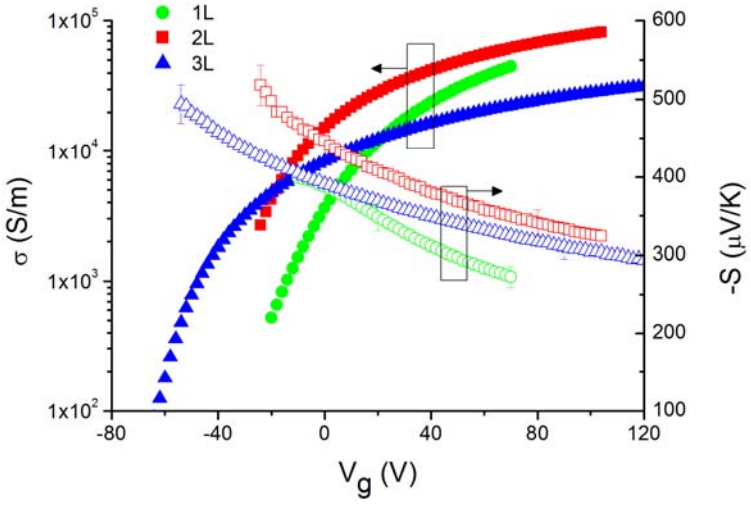

**FIG. 2.** Electrical conductivities, $\sigma$ (closed markers, error bars inclusive) and Seebeck coefficients, $S$ (open markers, error bars as indicated) as a function of gate voltage at 300 K for monolayer (green circles), bilayer (red squares) and trilayer $MoS_2$ (blue triangles). As the carrier concentration $n \propto (V_g - V_t)$ increases, $\sigma$ increases and the magnitude of $S$ decreases. $S$ is negative, which confirms that the sample is $n$-type.

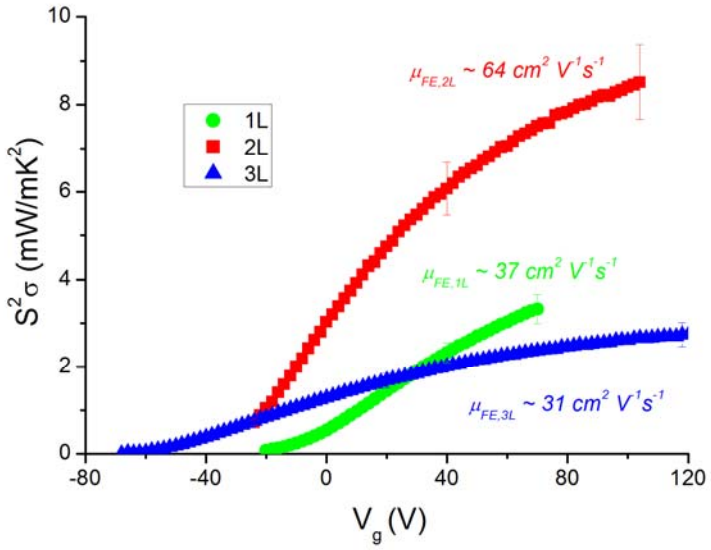


**FIG. 3.** Powerfactor, $S^2\sigma$ (representative error bars illustrated) as a function of $V_g$. The bilayer device with a larger effective mobility of 64 $cm^2V^{-1}s^{-1}$ exhibits maximum powerfactor of 8.5 $mWm^{-1}K^{-2}$ at $n$=1.06×10$^{13}$ $cm^{-2}$ at room temperature, twice that of commercially used bulk $Bi_2Te_3$.

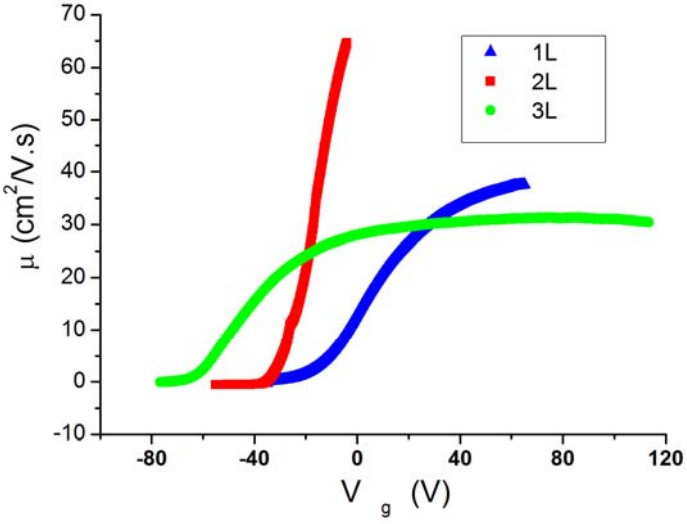

**FIG. 4.** The measured field-effect mobilities of monolayer, bilayer and trilayer as a function of back gate ($V_g$). The measured mobility is 37 $cm^2V^{-1}s^{-1}$ for the monolayer, 64 $cm^2V^{-1}s^{-1}$ for the bilayer and 31 $cm^2V^{-1}s^{-1}$ for the trilayer.

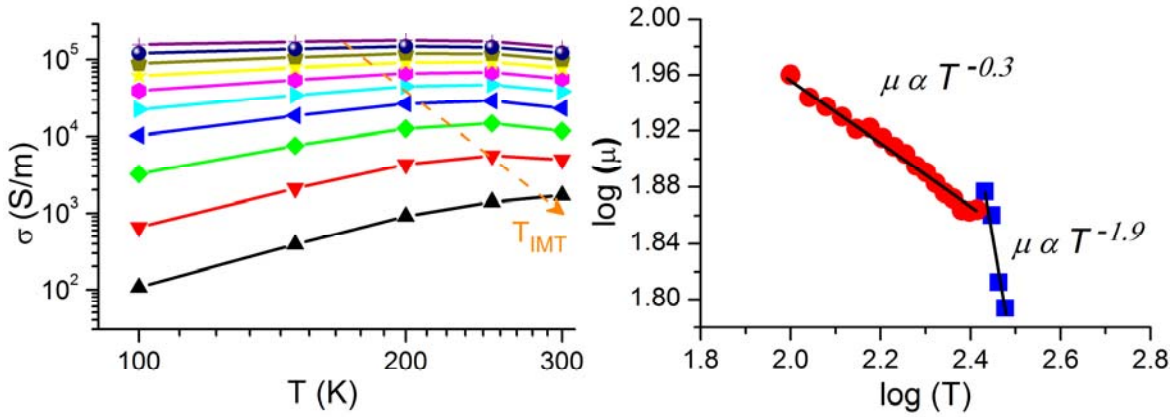


**FIG. 5.** (a) Conductivity as a function of temperature (high ($n = 5\times10^{12}$ $cm^{-2}$ at the top) to low ($n = 4\times10^{11}$ $cm^{-2}$ at the bottom) carrier concentration). As the gate voltage (carrier concentration) decreases, the insulator-to-metal transition temperature ($T_{IMT}$) shifts to higher temperatures (indicated by the dotted arrow). (a) Temperature-dependent mobility of monolayer $MoS_2$. The mobility undergoes a rapid decrease with an exponent ~0.3 to ~1.9 crossing the metal-insulator-transition temperature ($T_{IMT}$).

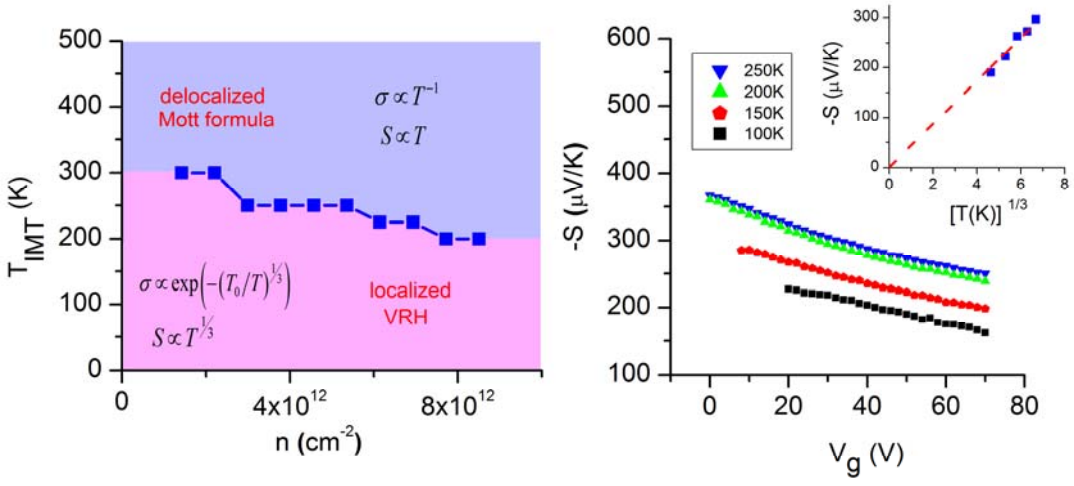


**FIG. 6.** (a) Phase diagram for thermoelectric transport as a function of temperature and electron concentration. For the metallic phase, $T > T_{IMT}$, electrical conductivity decreases with temperature, $\sigma \propto T^{-1}$ and the Seebeck coefficient increases slowly, $S \propto T$ (Mott formula for extended states). In the insulating phase, $T < T_{IMT,}$ Mott-Variable Range Hopping for localized states dictates transport resulting in $\sigma \propto \exp(-(T_0/T)^{1/3})$ (see Supplemental Material) and $S \propto T^{1/3}$. (b) Experimental Seebeck coefficient for monolayer $MoS_2$ as a function of temperature and applied back-gate voltage. The magnitude of Seebeck decreases (increases) with $V_g$ (temperature). In the inset we show measured Seebeck at a fixed carrier concentration $n = C_{ox}/e \cdot (V_g - V_t)$, which follows a function of $T^{1/3}$, indicating m-VRH (localized) regime in the temperature range 100-250 K (further details in Supplemental Material). At all temperatures, the experimental Seebeck at a fixed carrier concentration ($V_g$-$V_t$) is considered.

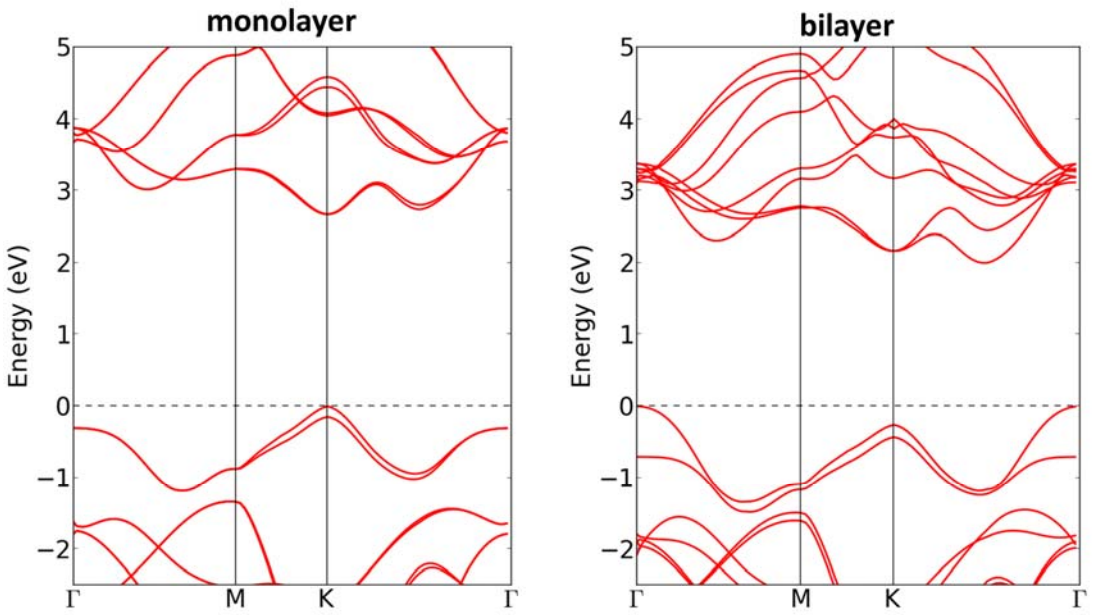


**FIG. 7.** Quasiparticle bandstructure of pristine monolayer (left) and bilayer (right) $MoS_2$ calculated at the GW level

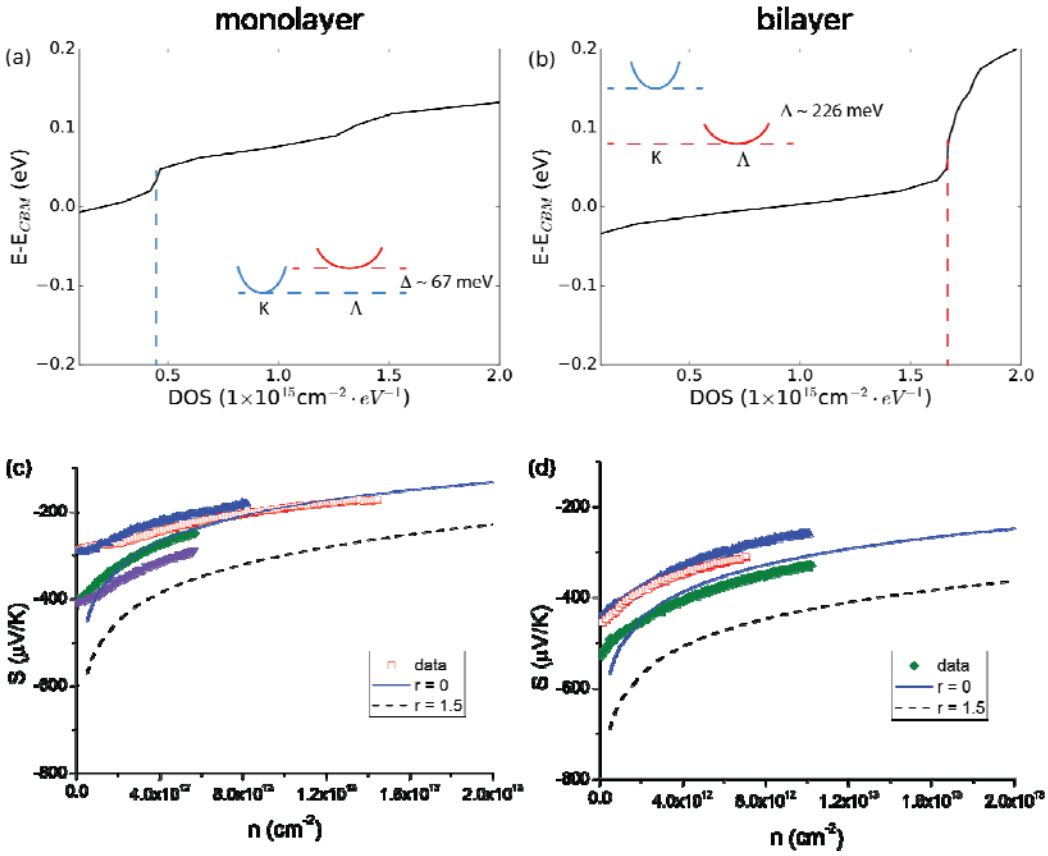


**FIG. 8.** Calculated DOS of pristine (a) monolayer and (b) bilayer $MoS_2$ plotted as a function of the energy difference from the conduction band minimum (CBM) in the K(Λ)-valley for the mono(bi)layer. The step function feature expected from 2D confinement can be seen clearly and is used to estimate the constant DOS (dotted vertical lines) used in Eq. (1). [inset: the relative positions of the K and Λ valleys in monolayer and bilayer $MoS_2$ showing that thermoelectric transport only occurs through the K-point in the monolayer and only through the Λ-high-symmetry direction in the bilayer, since the energy difference $>\sim 2k_BT$ in both cases]. (c) Monolayer and (d) bilayer experimental data (open symbols) compared with the estimated Seebeck coefficient from Eq. (1) for r=0, consistent with phonon-limited scattering in 2D, (solid lines) and r=1.5, for reference (dashed lines) – the data fits the r=0 phonon-limited scattering case well.

**Table I:** Comparison of 1. Difference between the conduction band minimum at K and along the Λ high-symmetry line ($E_K$-$E_\Lambda$), 2. SO splitting of the conduction band at K, and 3. effective masses for spin up (↑) and spin down (↓) states in the K and Λ valleys in units of the free electron mass ($m_0$) for monolayer and bilayer $MoS_2$ with different doping levels (n).

| | n ($cm^{-2}$) | $E_K$-$E_\Lambda$ (eV) | $E_{K,c\downarrow}$-$E_{K,c\uparrow}$ (eV) | $m_{K\uparrow}$ ($m_0$) | $m_{K\downarrow}$ ($m_0$) | $m_{\Lambda\uparrow}$ ($m_0$) | $m_{\Lambda\downarrow}$ ($m_0$) |
|---|---|---|---|---|---|---|---|
| monolayer | 0 | -0.067 | 0.003 | 0.45 | 0.59 | 0.87 | 0.73 |
| monolayer | $1x10^{13}$ | -0.668 | 0.003 | 0.45 | 0.53 | 1.18 | 1.02 |
| bilayer | 0 | 0.226 | 0.000 | 0.67 | 0.67 | 0.68 | 0.68 |

**Table II**. Summary of band structure calculations obtained from pristine monolayer and bilayer $MoS_2$ used for the estimation of the Seebeck coefficient using Eq. (1):

| | monolayer | bilayer |
|---|---|---|
| Valley Degeneracy: $g_v$ | 2 | 6 |
| Spin Degeneracy: $g_s$ | 2 | 2 |
| Effective Mass: $m^*$ | $(0.45+0.59)/2\ m_0 \sim 0.52m_0$<br>at the K-point CBM | $0.68m_0$<br>at the Λ-point CBM |
| Density of States, $D_{2D}$ | $4.33x10^{14}$ $cm^{-2}$ $eV^{-1}$ | $17.0x10^{14}$ $cm^{-2}$ $eV^{-1}$ |

## APPENDIX A
## Sample preparation and characterization and measurement details

Exfoliated samples are obtained using the scotch-tape method by cleaving bulk molybdenite. We exfoliate the samples onto 275 nm thermally grown $SiO_2$ on a highly doped *p*-Si substrates. $MoS_2$ flakes are visible on the sample under an optical microscope and the monolayer, bilayer or trilayer samples are selected based on characterization using optical contrast, photoluminescence imaging and Raman Spectroscopy (see Supplemental Material). Layer thicknesses for monolayer and bilayer devices are measured with Atomic Force Microscopy (AFM) for fabricated samples. Defective samples with cracks, ripples and/or folds are identified with High-Resolution Scanning Electron Microscopy (HR-SEM) and are not used for measurements (see Supplemental Material).

The heating element is a resistive metal line, through which a DC current, $I_{DC}$, up to 20 mA is applied. The heat generated from the heater line creates a temperature gradient across the TMDC sample, given by $Q \propto I^2_{DC} R_{htr} \propto \Delta T$. The electrodes patterned on two sides of the sample function both as probes for electrical measurements and for local temperature measurement. For each electrode, the resistance is given by $R_{hot/cold} \propto T_{hot/cold}$. Then, the temperature difference across the device is calibrated as $\Delta T = T_{hot} - T_{cold}$, where $R_{hot/cold} = \alpha_{hot/cold}/T_{holt/cold}$ obtained at every global temperature, where the slope $\alpha_{hot/cold}$ is determined experimentally. The open circuit voltage across the device, $V_{oc}$, as a function of heating current is then determined, from which the Seebeck coefficient of the device can be deduced as $S = -V_{oc}/\Delta T$.

In order to minimize the electrical contact resistance, we use Ti/Au films evaporated with electron beam evaporation. Titanium has been known to have good Fermi level alignment with monolayer $MoS_2$ [56]. In order to improve the contact quality, we annealed the sample *in-situ* at 475 K for one hour in the cryostat prior to performing measurements. After annealing, all of our *I-V* curves are linear, indicating ohmic contact and hence none of the transport characteristics can be ascribed to Schottky behavior. It has been reported that the contact resistance contribution to measured total resistance at room temperature can be as large as 50% at 100 K with Ti/Au contacts [56]. In our case, we define the ratio of the four-probe to the two-probe conductivity as the contact ratio, $\gamma_c$, which is 2 at 300 K and 2.5 at 100 K. Hence, our estimation of the intrinsic electrical conductivity of the layered $MoS_2$ is underestimated due to included contact resistance. The Seebeck measurements are not affected by the contact quality since they are measured in an open-circuit configuration. However, the measured *S* is a sum of the sample and the contacts (Ti/Au). Since the metallic Seebeck is < 1 $\mu VK^{-1}$ at all temperatures, it does not affect our measurements and we do not consider it in our estimation. The effects of joule heating, current crowding and thermoelectric potentials due to current flow in the 2D devices [57,58] is negligible since the current densities used for electrical conductivity measurements are very small, $I_{ds}$ < 0.1 μA/μm (see Supplemental Material). All measurements were performed in vacuum at $2\times10^{-6}$ torr. For lower gate voltages close to the threshold voltage $V_t$, the channel resistance becomes too high and we are unable to measure the Seebeck coefficient accurately. The maximum gate voltages $V_g$ applied for all devices are limited by the electrical breakdown of the gate oxide. In order to determine identical carrier concentrations (*n*) for different devices, we determined the threshold voltage ($V_t$) by linear extrapolation of the transfer curve ($I_{ds}$ vs $V_g$). Since each device has a different $V_t$, the gate voltage

at which the powerfactor is considered (for same carrier concentration) is also different for each device. The highly doped Silicon wafer (the backgate) acts as a heat sink that controls the temperature gradient across the two electrodes, while the low thermal conductivity $SiO_2$ (gate-dielectric) acts as a thermal barrier between the bottom wafer and the metal electrodes, controlling the actual local temperatures. The heat is generated from the center of the patterned heater and decays linearly on the surface of the $SiO_2$ upon which the $MoS_2$ lies, while the metal electrodes that function as resistance thermometers measure the local temperature gradient in intimate contact with the $MoS_2$ as described in Methods in detail. The heat flows out from the EBL-defined heater isotropically in all directions in the $SiO_2$ substrate. Since the $MoS_2$ is atomically thin, a very small portion of that heat generated by the heater actually flows through the $MoS_2$ cross-section. The key to accurate Seebeck measurement of the $MoS_2$ lies in measuring the local temperature across the $MoS_2$ at the same locations as the open-circuit voltage, which the design is able to accomplish. The high resistance in the OFF state of the $MoS_2$ ($V_g \leq V_t$) introduces additional capacitive coupling and hence the noise levels of the Seebeck measured are higher. We do not measure the Seebeck in the OFF state in this study.

**References:**


[1] C. Slack, in *CRC Handb. Thermoelectr. Ed. by D.M. Rowe* (CRC Press, Boca Raton, 1995), pp. 407–440.

[2] L.-D. Zhao, S.-H. Lo, Y. Zhang, H. Sun, G. Tan, C. Uher, C. Wolverton, V. P. Dravid, and M. G. Kanatzidis, Nature **508**, 373 (2014).

[3] A. I. Hochbaum, R. Chen, R. D. Delgado, W. Liang, E. C. Garnett, M. Najarian, A. Majumdar, and P. Yang, Nature **451**, 163 (2008).

[4] J. P. Heremans, V. Jovovic, E. S. Toberer, A. Saramat, K. Kurosaki, A. Charoenphakdee, S. Yamanaka, and J. G. Snyder, Science (80-. ). **321**, 554 (2008).

[5] D. M. Rowe, *Thermoelectrics Handbook: Macro to Nano* (Taylor & Francis, 2005).

[6] B. Radisavljevic, a Radenovic, J. Brivio, V. Giacometti, and a Kis, Nat. Nanotechnol. **6**, 147 (2011).

[7] Q. H. Wang, K. Kalantar-Zadeh, A. Kis, J. N. Coleman, and M. S. Strano, Nat. Nanotechnol. **7**, 699 (2012).

[8] T. Cao, G. Wang, W. Han, H. Ye, C. Zhu, J. Shi, Q. Niu, P. Tan, E. Wang, B. Liu, and J. Feng, Nat. Commun. **3**, 887 (2012).

[9] K. F. Mak, K. He, C. Lee, G. H. Lee, J. Hone, T. F. Heinz, and J. Shan, Nat. Mater. **12**, 207 (2013).

[10] D. Y. Qiu, T. Cao, and S. G. Louie, Phys. Rev. Lett. **115**, 1 (2015).

[11] W. Huang, X. Luo, C. K. Gan, S. Y. Quek, and G. Liang, Phys. Chem. Chem. Phys. **16**, 10866 (2014).

[12] D. Wickramaratne, F. Zahid, and R. K. Lake, J. Chem. Phys. **140**, 124710 (2014).

[13] H. Babaei, J. M. Khodadadi, and S. Sinha, Appl. Phys. Lett. **105**, 193901 (2014).

[14] B. Radisavljevic and A. Kis, Nat. Mater. **12**, 815 (2013).

[15] Z. Yu, Y. Pan, Y. Shen, Z. Wang, Z.-Y. Ong, T. Xu, R. Xin, L. Pan, B. Wang, L. Sun,

J. Wang, G. Zhang, Y. W. Zhang, Y. Shi, and X. Wang, Nat. Commun. **5**, 5290 (2014).

[16] W. Zhu, T. Low, Y.-H. Lee, H. Wang, D. B. Farmer, J. Kong, F. Xia, and P. Avouris, Nat. Commun. **5**, 3087 (2014).

[17] S. Kim, A. Konar, W.-S. Hwang, J. H. Lee, J. Lee, J. Yang, C. Jung, H. Kim, J.-B. Yoo, J.-Y. Choi, Y. W. Jin, S. Y. Lee, D. Jena, W. Choi, and K. Kim, Nat. Commun. **3**, 1011 (2012).

[18] K. Novoselov, A. Geim, S. Morozov, D. Jiang, Y. Zhang, S. Dubonos, I. Grigorieva, and A. Firsov, Science (80-. ). **306**, 666 (2004).

[19] A. H. C. Neto, F. Guinea, N. Peres, K. Novoselov, and A. Geim, Rev. Mod. Phys. **81**, 109 (2009).

[20] Y. Zuev, W. Chang, and P. Kim, Phys. Rev. Lett. **102**, 96807 (2009).

[21] F. Ghahari, H. Y. Xie, T. Taniguchi, K. Watanabe, M. S. Foster, and P. Kim, Phys. Rev. Lett. **116**, 1 (2016).

[22] Graphene, which is a prototypical 2D material, has exhibited larger powerfactors of ~10 $mWm^{-1}K^{-2}$ due to novel correlated effects but its thermoelectric applications are limited by an extremely high thermal conductivity.

[23] J. Wu, H. Schmidt, K. K. Amara, X. Xu, G. Eda, and B. Özyilmaz, Nano Lett. **14**, 2730 (2014).

[24] M. Buscema, M. Barkelid, V. Zwiller, H. S. J. Van Der Zant, G. A. Steele, and A. Castellanos-gomez, Nano Lett. **13**, 358 (2013).

[25] B. Bhushan, *Springer Handbook of Nanotechnology* (Springer, 2007).

[26] G. J. Snyder and E. S. Toberer, Nat. Mater. **7**, 105 (2008).

[27] K. Kaasbjerg, K. S. Thygesen, and K. W. Jacobsen, Phys. Rev. B **85**, 115317 (2012).

[28] S. Ghatak, A. N. Pal, and A. Ghosh, ACS Nano **5**, 7707 (2011).

[29] S. Lo, O. Klochan, C. Liu, W. Wang, A. R. Hamilton, and C.-T. Liang, Nanotechnology **25**, 375201 (2014).

[30] B. Baugher, H. O. H. Churchill, Y. Yang, and P. Jarillo-herrero, Nano Lett. **13**, 4212 (2013).

[31] P. Zvyagin, Phys. Status Solidi **58**, 443 (1973).

[32] S. V. Demishev, M. V. Kondrin, a. a. Pronin, N. E. Sluchanko, N. a. Samarin, a. G. Lyapin, and G. Biscupski, J. Exp. Theor. Phys. Lett. **68**, 842 (1998).

[33] M. J. Burns and P. M. Chaikin, J. Phys. C Solid State Phys. **18**, L743 (1985).

[34] B. Jalan and S. Stemmer, Appl. Phys. Lett. **97**, 42106 (2010).

[35] K. P. Pernstich, B. Rössner, and B. Batlogg, Nat. Mater. **7**, 321 (2008).

[36] T. Ando, A. B. Fowler, and F. Stern, Rev. Mod. Phys. **54**, 437 (1982).

[37] M. S. Hybertsen and S. G. Louie, Phys. Rev. B **34**, 5390 (1986).

[38] A. Splendiani, L. Sun, Y. Zhang, T. Li, J. Kim, C.-Y. Chim, G. Galli, and F. Wang, Nano Lett. **10**, 1271 (2010).

[39] H. P. Komsa and A. V. Krasheninnikov, Phys. Rev. B - Condens. Matter Mater. Phys. **86**, 1 (2012).

[40] A. Molina-Sanchez, D. Sangalli, K. Hummer, A. Marini, and L. Wirtz, Phys. Rev. B **88**, 1 (2013).

[41] D. Y. Qiu, F. H. Da Jornada, and S. G. Louie, Phys. Rev. Lett. **111**, 216805 (2013).

[42] D. Y. Qiu, F. H. da Jornada, and S. G. Louie, Phys. Rev. B **93**, 235435 (2016).

[43] J. M. Ziman, *Electrons and Phonons: The Theory of Transport Phenomena in Solids* (Clarendon, Oxford, 1960).

[44] E. H. Hwang, E. Rossi, and S. Das Sarma, Phys. Rev. B - Condens. Matter Mater. Phys. **80**, 1 (2009).

[45] N. Mohankumar and A. Natarajan, Phys. Status Solidi **188**, 635 (1995).

[46] X. Li, J. T. Mullen, Z. Jin, K. M. Borysenko, M. Buongiorno Nardelli, and K. W. Kim, Phys. Rev. B - Condens. Matter Mater. Phys. **87**, 115418 (2013).

[47] D. M. Rowe, *Materials, Preparation, and Characterization in Thermoelectrics* (Taylor & Francis, 2012).

[48] Y. Pei, X. Shi, A. LaLonde, H. Wang, L. Chen, and G. J. Snyder, Nature **473**, 66 (2011).

[49] T. Tritt, *Recent Trends in Thermoelectric Materials Research: Part Three* (Elsevier Science, 2001).

[50] P. Norouzzadeh, C. W. Myles, and D. Vashaee, Sci. Rep. **4**, 7028 (2014).

[51] D. Ovchinnikov, A. Allain, Y.-S. Huang, D. Dumcenco, and A. Kis, ACS Nano **8**, 8174 (2014).

[52] L. Li, Y. Yu, G. J. Ye, Q. Ge, X. Ou, H. Wu, D. Feng, X. H. Chen, and Y. Zhang, Nat. Nanotechnol. **9**, 372 (2014).

[53] S. J. Choi, B.-K. Kim, T.-H. Lee, Y. H. Kim, Z. Li, E. Pop, J.-J. Kim, J. H. Song, and M.-H. Bae, Nano Lett. **16**, 3969 (2016).

[54] S. Sinha and K. E. Goodson, Int. J. Multiscale Comput. Eng. **3**, 107 (2005).

[55] M. Kayyalha, J. Maassen, M. Lundstrom, L. Shi, and Y. P. Chen, J. Appl. Phys. **120**, (2016).

[56] B. W. H. Baugher, H. O. H. Churchill, Y. Yang, and P. Jarillo-herrero, Nano Lett. **13**, 4212 (2013).

[57] K. L. Grosse, M.-H. Bae, F. Lian, E. Pop, and W. P. King, Nat. Nanotechnol. **6**, 287 (2011).

[58] M. Bae, Z. Ong, D. Estrada, and E. Pop, Nano Lett. **10**, 4787 (2010).